Transition zone velocity gradients and the 520-km discontinuity

Peter M. Shearer

Institute of Geophysics and Planetary Physics, Scripps Institution of Oceanography, University of California, San Diego, La Jolla

Abstract.
Stacks of long-period Global Digital Seismograph Network (GDSN) seismograms at 110°
to 180° epicentral distance reveal precursors to SS that result from underside reflections
off upper mantle seismic discontinuities. The 410- and 660-km discontinuities are obvious
in these stacks, but identification and modeling of other transition zone discontinuities
are complicated by sidelobes from the 410- and 660-km reflections. These sidelobes
result from the limited bandwidth of the GDSN instrument responses and the effect of
crustal reverberations on the SS reference phase. The crustal effects can be minimized
by restricting the records to oceanic bounce points where the ~6-km-thick crust has
little effect on the long-period waveforms. Over 2000 long-period, transverse-component
seismograms with oceanic SS bounce points recorded by the GDSN from 1976 to 1991
are manually edited, aligned on SS, and then stacked using a new procedure that weights
the records by data quality. The resulting image shows a clear reflection from a 520-km
discontinuity that cannot be explained as a sidelobe artifact, confirming earlier results of
Shearer [1990, 1991] and *Revenaugh and Jordan* [1991]. By stacking along the expected
travel time curves for discontinuity phases, the time versus range image of the precursor
wave field is reduced to a single trace that measures upper mantle reflectivity versus time.
The features in this reflectivity profile are sensitive to the brightness and depth of the
transition zone discontinuities and to the steepness of the velocity gradients between the
interfaces. Using geometrical ray theory and assuming a constant velocity versus density
scaling relationship, I fit this reflectivity profile with velocity models of the upper mantle
using both forward modeling and direct inversion. The inverse problem is addressed by
performing a deconvolution of the profile with the SS reference phase (after a correction for
attenuation), followed by a direct mapping of reflectivity versus time into velocity versus
depth. Velocity-depth profiles resulting from these procedures are roughly in agreement
with standard upper mantle velocity models, except that the SS precursor data require a
minor discontinuity near 520 km and a steeper gradient just below the 660-km discontinuity.
Estimated discontinuity shear impedance changes are 6.7 ± 1.1% at 420 km, 2.9 ± 0.7% at
519 km, and 9.9 ± 1.5% at 663 km. The impedance change near 520 km is consistent with
current mineral physics results for the olivine β to γ phase change and places constraints
on the fraction of olivine in the transition zone.

Introduction

Unraveling the structure of Earth's upper mantle
transition zone has long been a challenge for seismologists. Traditional travel time analyses of refracted
arrivals are complicated by strong lateral heterogeneity in the upper mantle and by velocity discontinuities near 410 and 660 km depth that cause triplications in the travel time curves [e.g., *Niazi and Anderson*, 1965; *Johnson*, 1967]. Velocity structure immediately above and below these discontinuities is particu-

larly hard to resolve, since rays turning at these depths
do not produce first arrivals. The depth and sharpness of the discontinuities themselves are also difficult
to measure accurately with refracted arrivals. Recently,
many researchers have begun analyzing secondary seismic phases that result from reflections and phase conversions at upper mantle velocity discontinuities; these
studies provide valuable new constraints on the depth,
strength, sharpness, and topography of these boundaries [e.g., *Kind and Vinnik*, 1988; *Paulssen*, 1988;
Revenaugh and Jordan, 1989, 1991; *Davis et al.*, 1989;
Richards and Wicks, 1990; *Shearer*, 1990, 1991, 1993;
Bock and Kind, 1991; *Vidale and Benz*, 1992; *Benz
and Vidale*, 1993; *Wicks and Richards*, 1993; *Zhang and
Lay*, 1993].

Precursors to SS produced by underside reflections off upper mantle discontinuities can be used to map the global distribution and depth of these reflectors. However, because the precursors are generally very weak, stacking techniques are required to bring them above the noise. This has been done using long-period Global Digital Seismograph Network (GDSN) data in a series of studies [*Shearer* 1990, 1991, 1993; *Shearer and Masters*, 1992] analyzing SS precursors and other discontinuity phases that have produced global maps of the large-scale topography on the 410- and 660-km interfaces. These maps indicate about 30 to 40 km of peak-to-peak topography on the discontinuities and a prominent trough in the 660-km discontinuity near the subduction zones in the NW Pacific. The stacked images also suggest the presence of a minor impedance increase near 520 km depth. Recently, *Bock* [1994] performed a synthetic stacking experiment which indicated that the apparent 520-km phases seen in long-period stacked images may be sidelobe artifacts of the 410-km phase and require no structure at 520 km, thus disputing the contention of *Shearer* [1990, 1991] that sidelobe effects were unlikely to be responsible for the 520-km phases.

This paper focuses on using SS precursors to resolve details in transition zone velocity structure, with particular attention to the 520-km discontinuity, and is a continuation of my previous long-period stacking experiments. Improvements include an expanded data set, more careful editing and picking of the data, and a new stacking procedure that weights the records by their quality. Unlike much of my prior work, no attempt is made here to resolve lateral variability in structure; rather, the goal is to achieve the highest possible resolution of the average one-dimensional velocity structure in the transition zone. To avoid problems related to the distortion of long-period waveforms from passage through the crust, the analysis is restricted to oceanic SS bounce points, where the thin crust has little effect. The results show clear evidence for a 520-km reflector that cannot be explained as a sidelobe artifact of either the 410- or 660-km discontinuity phases. The final section of the paper will show upper mantle velocity versus depth profiles obtained from the SS precursor stack, using both forward and inverse modeling methods.

SS Precursors and the Effect of the Crust

The ray geometries for SS precursors resulting from underside reflections off the 410- and 660-km discontinuities are shown in Figure 1, at source-to-receiver ranges of 120°, 140°, and 160°. These phases are termed SdS, where d is the reflector depth (e.g., $S410S$ is the underside reflection from the 410-km discontinuity). Because the ray paths for SdS and SS are similar away from the SS bounce point, it makes sense to use SS as a reference phase to normalize the time and ampli-
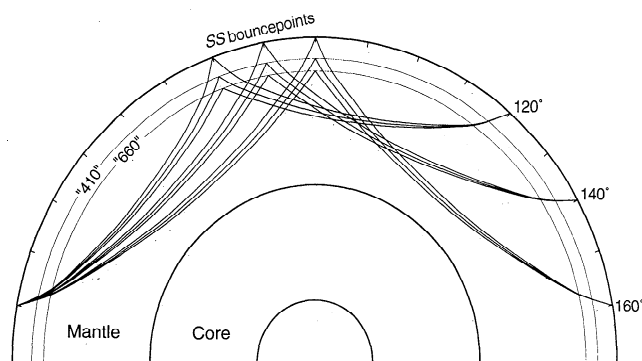

Figure 1. Ray paths of SS and the underside precursors $S410S$ and $S660S$ at source-receiver ranges of 120°, 140°, and 160°.

tude of the precursors. The timing of SdS relative to SS is related to the two-way travel time between the discontinuity and the surface, while the amplitude of SdS relative to SS is determined largely by the reflection coefficient at the interface. However, the shapes of the SdS and SS pulses are not identical; the SS pulse is more attenuated owing to extra paths through the uppermost mantle and is distorted by propagation through the crust. Attenuation reduces the amplitude of the pulses and broadens them slightly; the crustal operator is more significant since it affects the relative shape and sidelobe amplitudes of the SS wavelet.

The influence of the crust on a surface-reflected pulse is illustrated, to first order, in Figure 2. For an incident delta function, the underside Moho reflection is posi-
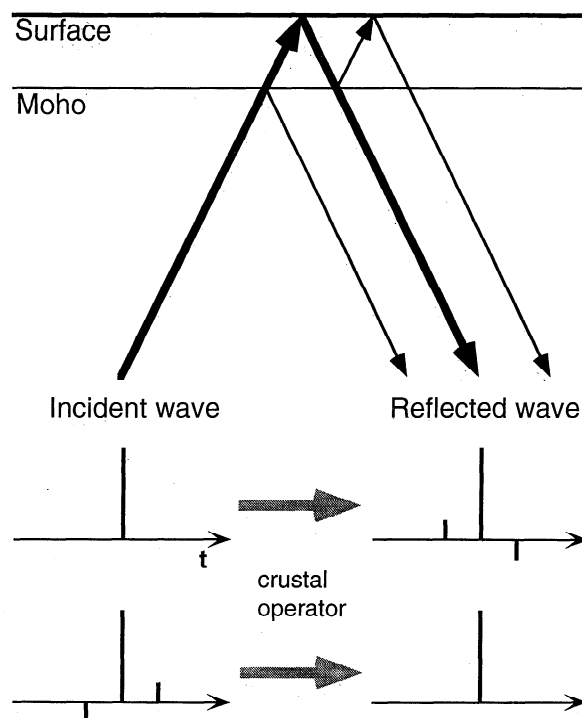

Figure 2. A cartoon illustrating the effect of the crust on surface-reflected pulses. Both underside and topside reflected pulses are generated at the Moho.

tively polarized and arrives in front of the main pulse, while the first topside Moho reverberation is opposite in polarity and arrives after the main pulse (higher-order crustal reverberations are much smaller in amplitude and can generally be ignored). An inverse crustal operator may also be defined as the incident pulse that will result in a delta function reflected pulse. Figure 2 plots an approximation to the inverse operator, again ignoring higher-order terms. The precise form of these operators depends upon the ray parameter, the Moho impedance contrast, and the thickness and average velocity of the crust.

Figure 3 illustrates the result of applying these crustal operators to a typical reference wavelet (obtained by stacking long-period SS arrivals), using a Moho reflection coefficient of 0.17 and travel times appropriate for vertical S wave propagation through a crust of varying thickness. Crust less than about 10 km thick (oceanic) has little effect on the wavelet, while crustal thicknesses greater than about 20 km (continental) lead to significant pulse distortion, with the forward operator increasing the amplitude of the sidelobes following the main peak and the inverse operator increasing the amplitude of the precursory sidelobes. The forward operator predicts the shape of wavelets with an extra surface bounce compared to the reference phase (i.e., topside multiples following S, such as $Ss410s$); the inverse operator predicts the shape of pulses with one less surface bounce than the reference phase (i.e., SS precursors such as $S410S$). The effect and importance of crustal operators were noted by *Revenaugh and Jordan* [1989] in their studies of long-period ScS reverberations.

The synthetic stacked images obtained by *Bock* [1994] were computed using a uniform 35-km-thick crust, and their oscillatory appearance (high-amplitude sidelobes for the discontinuity phases) is likely due to these crustal operators. The data stacks given by *Shearer* [1990, 1991] are less affected by the crust, since most of the ray paths have oceanic bounce points. This can be seen by comparing the amplitude of the sidelobes around the 660-km phase between the data stacks and the synthetic stacks [see *Bock*, 1994, Plates 1–3]. The 660-km sidelobes are much smaller in the data stacks than in Bock's synthetics, indicating a reduced influence of the crust on pulse shapes in the data stacks as compared to the synthetics.

Sidelobe amplitudes play a critical role in evaluating whether apparent 520-km reflections in the data stacks are real, since the 520-km phases arrive near sidelobes of the 410-km reflections in all three cases where they have been observed (i.e., topside reflections following P and S and underside reflections preceding SS; see *Shearer* [1991]). *Bock* [1994] argues that the 520-km features in the data stacks are a sidelobe artifact of the 410-km reflections, since the 410-km sidelobes in his synthetic stacks (computed for a model with no structure at 520 km) are comparable in amplitude to the 520-km features in the data. However, it appears that the sidelobes in
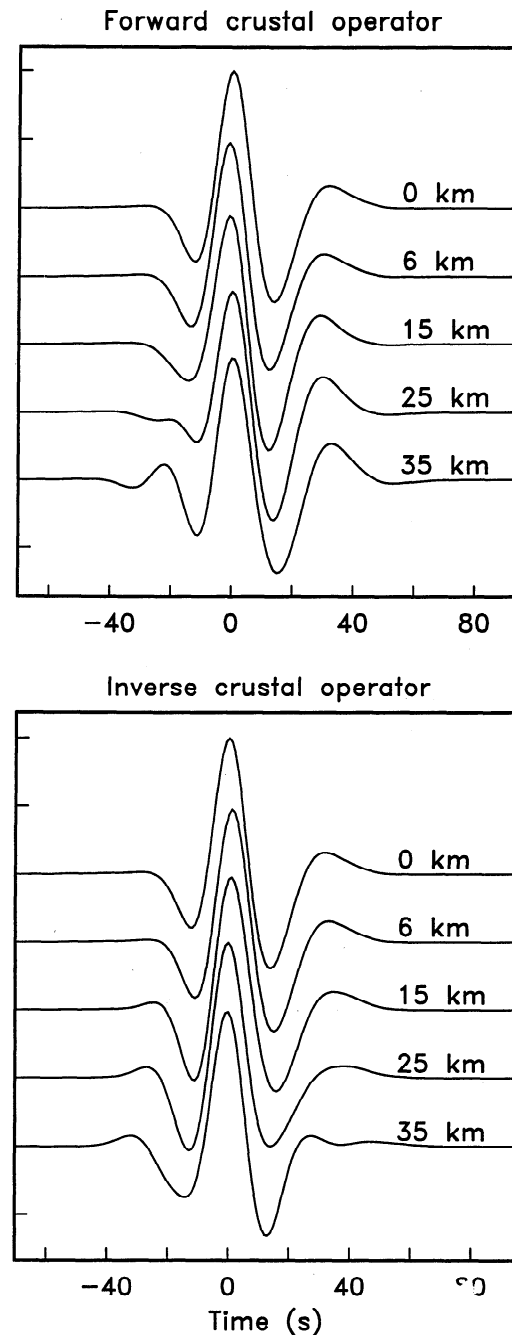

Figure 3. The effect of forward and inverse crustal operators on a long-period reference wavelet, assuming vertical incidence and a Moho reflection coefficient of 0.17. While 6-km-thick crust (i.e., oceanic) has virtually no effect on the wavelet, 25- to 35-km-thick crust (i.e., continental) causes significant distortion in the pulse and changes the sidelobe amplitudes.

his synthetic stacks are exaggerated compared to the data, so this comparison is of questionable relevance. As discussed by *Shearer* [1990, 1991], it is the prominence of the 520-km phases and the lack of similar features near the 660-km reflector that indicate that the 520-km arrivals are real and not sidelobe artifacts of the 410-km discontinuity.

Although it is possible to correct for the effect of the crust in long-period stacks, these corrections are subject

to some uncertainty since crustal thickness is not always known precisely, particularly on continents where the correction is most important. To reduce these uncertainties and obtain the highest possible resolution of the amplitude and shape of upper mantle reflectors, the SS results described here are obtained using only oceanic SS bounce points, where the thin crust has virtually no effect on the long-period waveforms (see Figure 3). The data coverage is shown in Figure 4, where SS bounce points are plotted for 2006 seismograms obtained from the GDSN and the Incorporated Research Institutions for Seismology Global Seismograph Network (IRIS GSN) between 1976 and 1991, at source-receiver ranges of 110° to 180°. To avoid complications due to depth phases, analysis is restricted to events less than 75 km deep.

Stacking Procedure

The stacking procedure is similar to that described by *Shearer* [1991], to which the reader is referred for more details. However, a few improvements have been made; these include manual editing of the data, more consistent alignment of SS prior to stacking, and weighting of the records by apparent signal-to-noise levels. Figure 5 shows one of the transverse-component seismograms used in the stack, in this case for a rare example in which apparent transition zone precursors to SS are suggested in an individual record. The data are edited to exclude noisy traces and multiple or complicated SS waveforms. To reduce the size of precursory sidelobes, the first major swing in SS is picked as an alignment
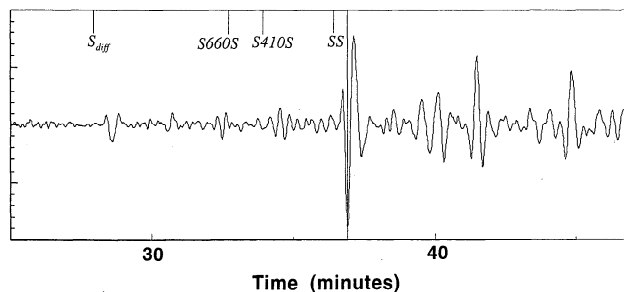
1989 145 00:54 ANMO   118.8°

Figure 5. An individual transverse-component seismogram from station ANMO at a range of 118.8°. The predicted arrival times of SS and the precursory phases $S410S$ and $S660S$ are indicated at the top of the plot.

point, rather than the peak SS amplitude as in the results of *Shearer* [1990, 1991]. Negative polarity pulses are reversed prior to stacking.

The expected amplitudes of the discontinuity phases (e.g., $S410S$, $S660S$, etc.) are only a few percent of the amplitude of SS. This is below the incoherent "noise" levels prior to SS on the vast majority of the seismograms; it is only by stacking a large number of records that the SdS phases can be seen reliably. My previous stacks [*Shearer*, 1990, 1991] normalized the amplitude of each trace to the SS peak amplitude prior to stacking. This has the undesirable effect of giving the most weight to the seismograms with the highest precursory amplitudes. In the current procedure, a local signal-to-noise parameter is computed for each seismogram as the ratio of the peak SS amplitude to the peak amplitude in a 5-min window prior to SS. The traces are normal-
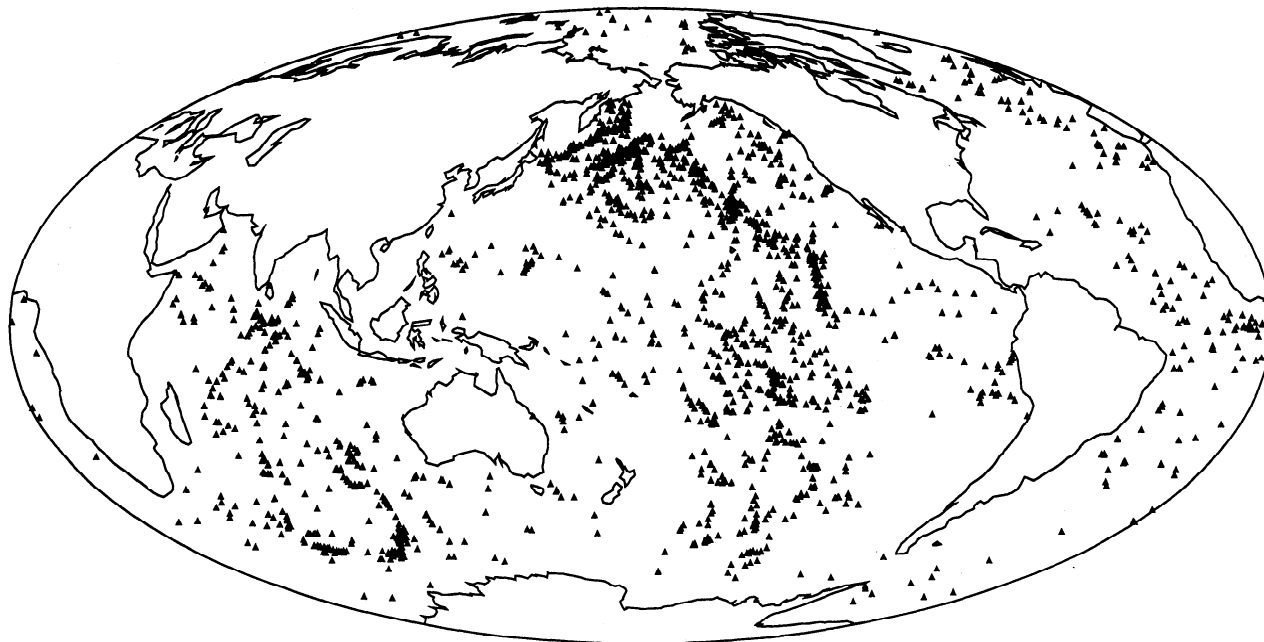

Figure 4. The SS bounce point locations for the 2006 long-period seismograms used in this study. Only oceanic regions are sampled, where the thin crust causes little distortion in long-period SS waveforms.

ized to the amplitude in this precursory window and weighted by the apparent signal-to-noise. (In practice the results are not particularly sensitive to the choice of weighting procedure, and similar waveforms are obtained in stacks with different apparent signal-to-noise levels.)

Plate 1 shows the image resulting from stacking SS in 1° range bins between 110° and 180°, while Figure 6 plots corresponding travel time curves for the visible phases, computed using the IASP91 velocity model [*Kennett*, 1991]. SS is shifted to zero time and normalized to unit amplitude. Positive amplitudes are blue, and negative amplitudes are red. The major arrivals, such as SS, SSS, $ScSScS$ and S_{diff}, are saturated, since the peak amplitude in the plot is just 5% of the amplitude of SS. The $S410S$ and $S660S$ underside re-

flections are clearly apparent, arriving 2.5 to 4 min before SS. As in the previous stacks of *Shearer* [1991] and *Shearer and Masters* [1992], there is evidence for another phase between $S410S$ and $S660S$, the 520-km underside reflection $S520S$. Figure 7 plots the number of traces combined in each 1° bin to form the image shown in Plate 1. Generally, there are more traces available at closer ranges and very few data available near the antipode at 180°; this is reflected in the noisier appearance of the stacked image at ranges beyond 160°.

The close visual agreement between the observed and predicted $S410S$ and $S660S$ travel times provides strong confirmation of the existence of the 410- and 660-km reflectors. However, quantitative exploration of more subtle features in Plate 1, such as the possible 520-km reflector, is more difficult, and amplitudes are
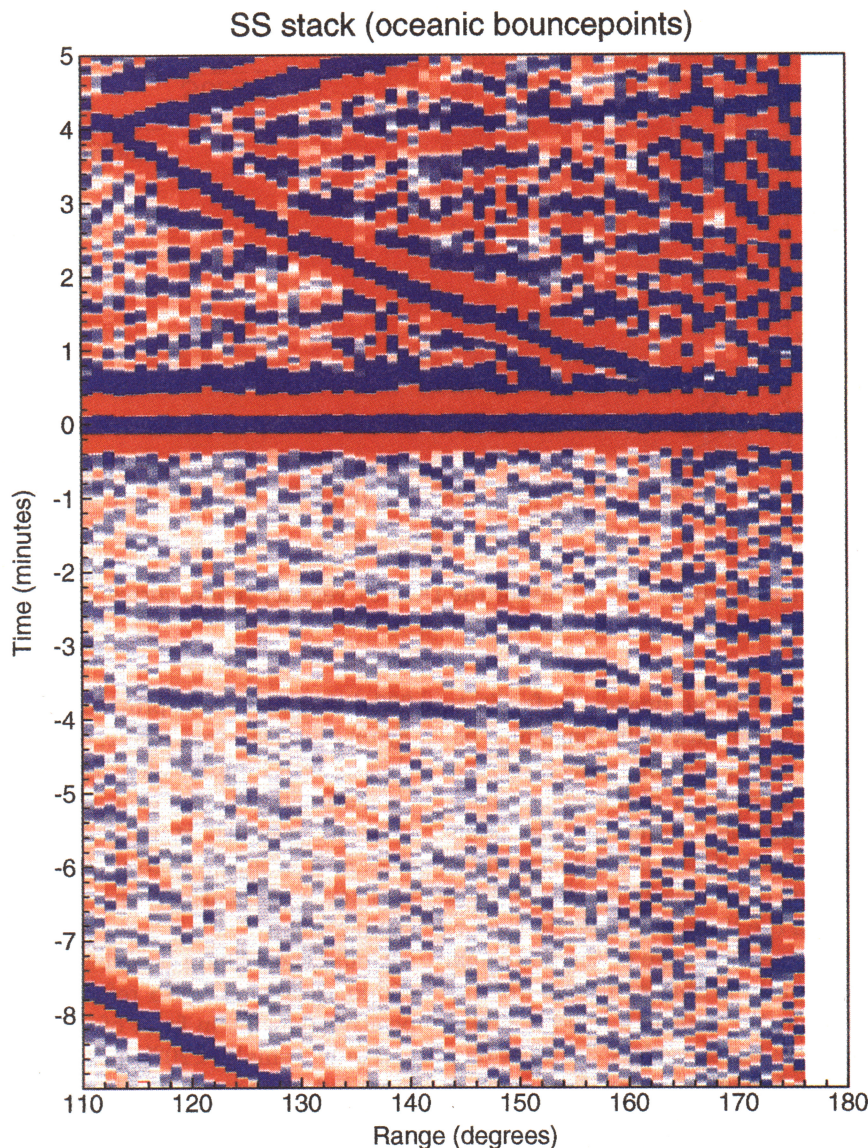

Plate 1. A time versus range image showing SS and its precursors obtained by stacking 2006 individual long-period seismograms. Positive amplitudes are blue, and negative amplitudes are red. The scale ranges from -0.05 to 0.05 of the amplitude of SS which is normalized to unit amplitude.
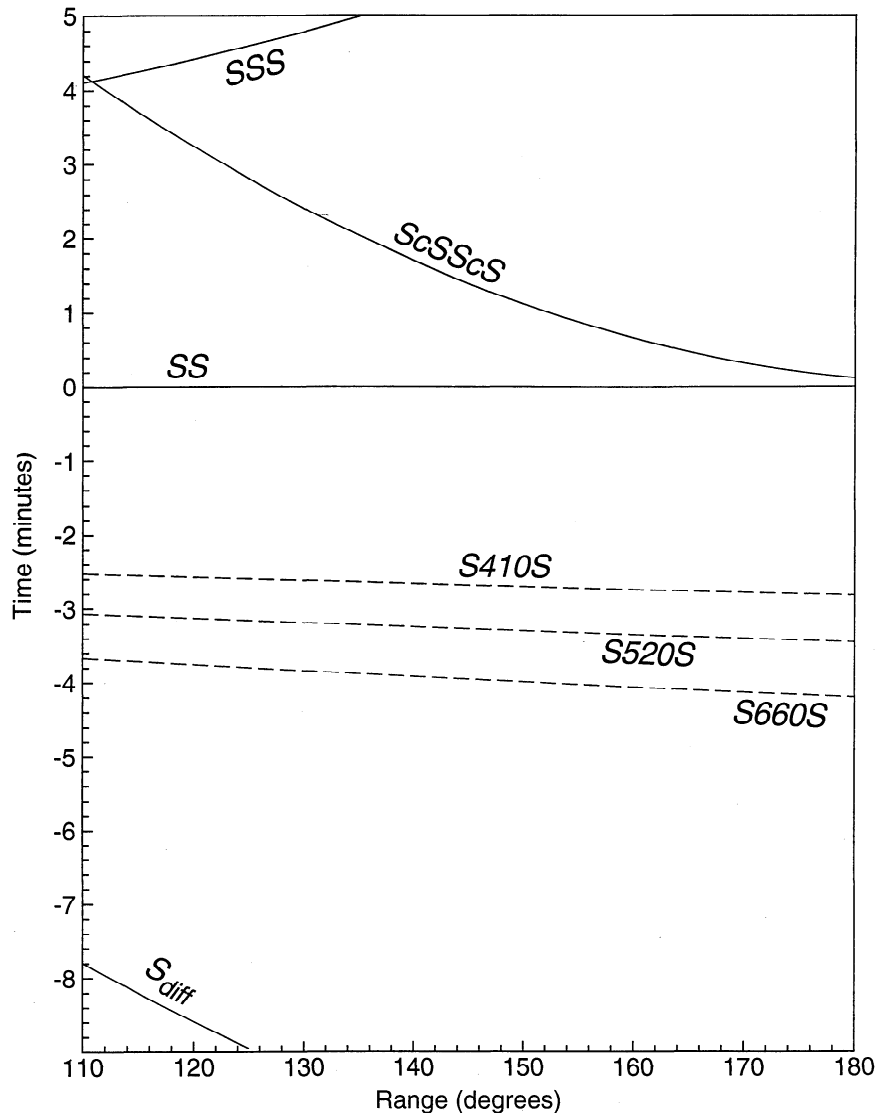
Figure 6. Predicted travel time curves for the IASP91 velocity model corresponding to the data stack shown in Plate 1.

hard to measure directly from the image. To facilitate additional analysis, I combine data from range bins between 120° and 160° to produce a single stacked trace. The result, shown in Figure 8, is obtained by stacking the SdS phases along the theoretical travel time curve for $S550S$ (the 550 km depth is arbitrary and is used to give a travel time curve nearly parallel to both $S410S$ and $S660S$), with the timing adjusted to a reference range of 138° (the average range of the individual traces). The reference pulse is obtained separately by stacking SS. Peaks from the 410- and 660-km reflections are clear in Figure 8; the secondary peak between these two features is the 520-km reflector.

The Robustness of the 520-km Peak

How significant is the 520-km phase seen in this composite stack? To obtain statistical error bounds, the traces are randomly resampled and the stack repeated

200 different times to provide a bootstrap estimate [e.g., *Efron and Tibshirani*, 1991] of the standard errors. The thin lines in Figure 8 show the 95% confidence limits of the estimate. Peaks from reflectors at 410, 520, and 660 km are clearly statistically significant and not random fluctuations due to undersampling (however, note that the small peaks at other depths are only marginally significant).

Could the 520-km peak be a sidelobe of the 410- and 660-km peaks? The SS reference pulse has virtually no positive sidelobe in front of the main three-swing pulse and only a small ($<20\%$) positive sidelobe following the main pulse, whereas the 520-km peak is almost half the size of the 410- and 660-km peaks. Since only oceanic bounce points are used, the SS pulse shape should be relatively undistorted compared to the precursory waveforms (see above). An excellent fit to the 410- and 660-km wavelets may be obtained by scaling and shifting the SS pulse (Figure 9a); when the 410- and 660-km
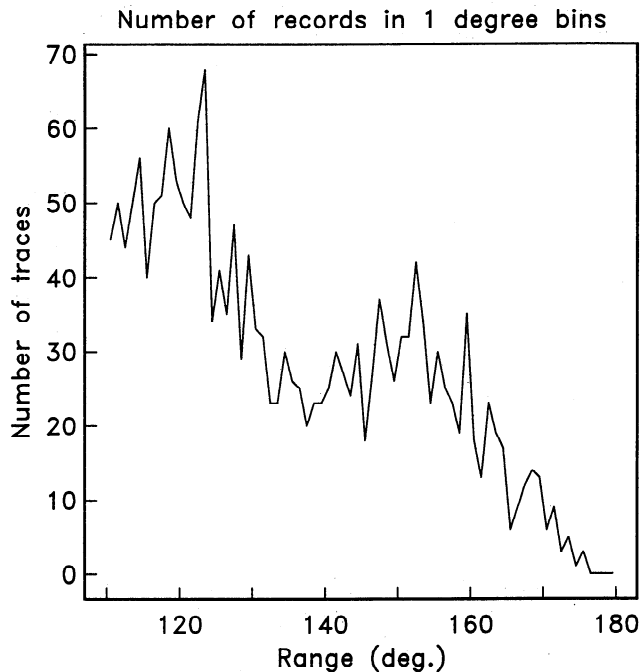
Number of records in 1 degree bins

Figure 7. A histogram of the number of seismograms stacked within each 1° range bin used in Plate 1.

peaks are subtracted, the 520-km peak becomes more prominent (Figure 9b). Another feature that appears significant in these plots is the trough that precedes the 660-km peak; the trough is wider and shallower in the data stack than is predicted by the shape of the reference pulse. As shown in the next section, the shape of
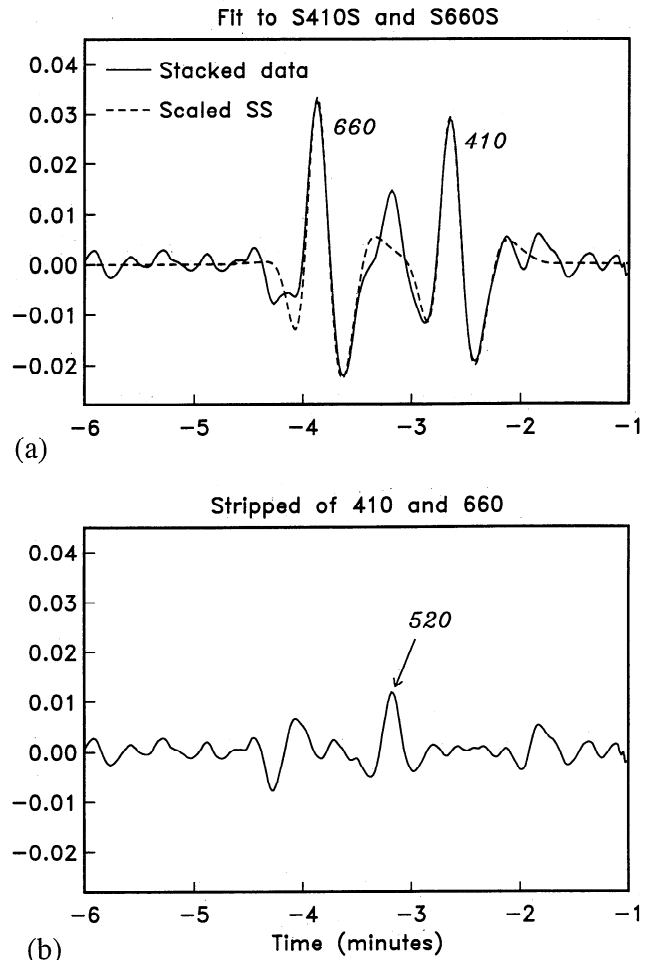
SS Precursor Stack (oceanic bouncepoints)

Figure 8. A stack of SS precursors in 1142 seismograms between 120° and 160° range, showing peaks from the underside reflected phases $S660S$ and $S410S$. The precursors are stacked along the predicted travel time curve for a reflector at 550 km and adjusted to a reference range of 138°. SS is stacked separately and scaled to unit amplitude; the precursor amplitudes are exaggerated by a factor of 10 for plotting purposes. The 95% confidence limits, shown as thin lines, are calculated using a bootstrap technique that randomly resamples the traces before stacking. Note the peak between the 410- and 660-km peaks, suggesting an additional reflector at 520 km depth.

Fit to S410S and S660S

Stripped of 410 and 660

Figure 9. (a) The dashed line shows the fit to the SS precursor stack obtained by scaling the SS reference pulse to fit the 410- and 660-km peaks. Note the good fit to these peaks but the misfit of the 520-km peak and the precursory sidelobe to the 660-km peak. (b) The remaining signal in the SS precursor stack after the fit to the 410- and 660-km peaks is subtracted from the trace.

this trough results from a steep velocity gradient immediately below the 660-km discontinuity.

The slight bump shown in Figure 9b at about -1.8 min corresponds to a discontinuity depth of 280 km. It is possible that this represents the "X" discontinuity hypothesized by *Revenaugh and Jordan* [1991] to explain results for some of their ScS reverberation profiles. However, the amplitude of this feature is only marginally significant when compared to the size of the error bounds plotted in Figure 8, and SS precursor results from different regions [*Shearer*, 1993] do not suggest a globally coherent reflector near 280 km.

Is the 520-km reflector a global feature or specific to a few isolated regions? Figure 10 compares separate SdS stacks from northern hemisphere and southern hemisphere bounce points; the 520-km peak is resolved in both. Stacks at different range intervals (not shown) also consistently show the 520-km peak. Previous SS stacking results have found evidence for the 520-km
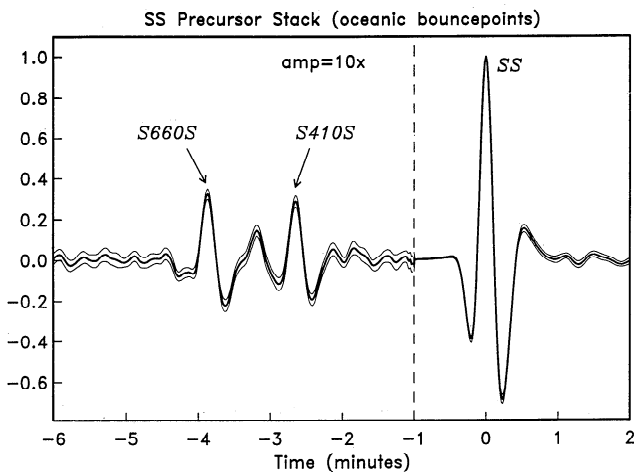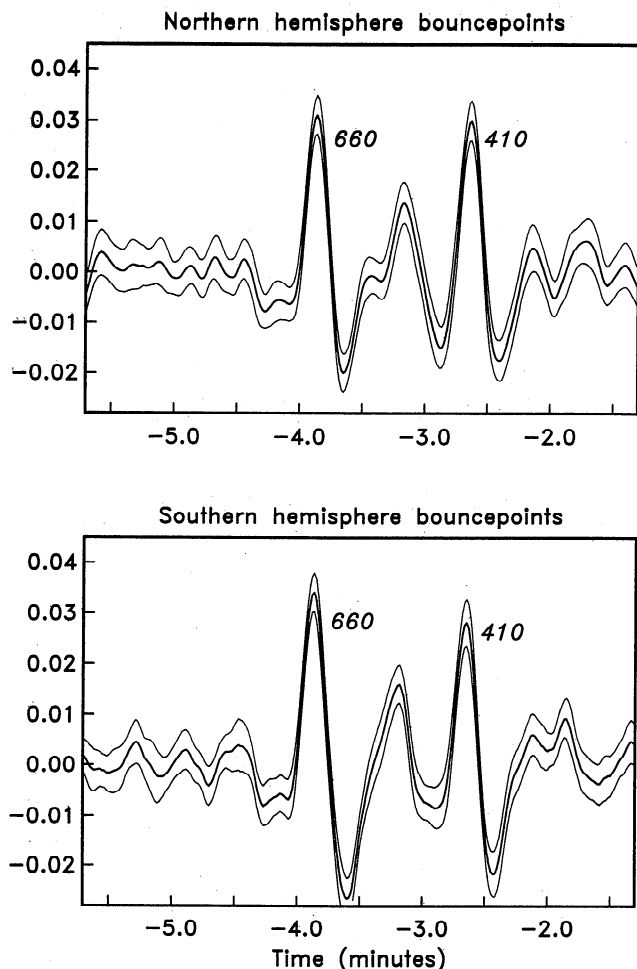
Figure 10. Separate stacks from 645 northern hemisphere and 497 southern hemisphere SS bounce points, showing the consistency of the 520-km peak.

reflector in both continental and oceanic regions [e.g., *Shearer*, 1991, Figure 16; *Shearer*, 1993, Figure 18]. It is not my purpose here to repeat this work, other than to reemphasize that the 520-km phase is not a sidelobe artifact of the stacking method. Long-period 520-km reflections appear to be a consistent global feature, observed wherever sufficient data are available.

Forward Modeling for v(z)

SS precursors provide valuable constraints on the shear velocity structure of the transition zone, since their timing, amplitude, and shape can be predicted using synthetic seismogram modeling. This section describes the forward problem of computing SS precursor waveforms from an upper mantle velocity model. Since there are no triplications, caustics, or diffracted waves in either the SS or SdS arrivals at ranges between 120° and 160°, ray theory provides a good first-order technique. Figure 11 illustrates the steps involved in producing $S(t)$ from $V_s(z)$, where $S(t)$ is the predicted SS precursor time series and V_s is the S velocity at depth z. Assuming SS propagation at a target range, ray theory

can be used to map from $V_s(z)$ to $V_s(t)$. This gives the arrival time for a precursory reflection from a discontinuity at any depth in the model. The next and most complicated step is to compute the amplitude of these reflections as a function of time.

In order to do this, we must compute the reflection coefficient at each time step. If the digitization interval is dt, the SH reflection coefficient R at time t_0 may be computed from the velocities and ray angles at $t_0 - dt/2$ and $t_0 + dt/2$

$$R(t_0) = \frac{\beta_2^2 \cos\theta_2 - \beta_1^2 \cos\theta_1}{\beta_2^2 \cos\theta_2 + \beta_1^2 \cos\theta_1}$$

where $\beta_1 = V_s(t_0 + dt/2)$, $\beta_2 = V_s(t_0 - dt/2)$, θ_1 is the ray angle at $t_0 + dt/2$, and θ_2 is the ray angle at $t_0 - dt/2$. Note that the dependence on density, normally in reflection coefficient formulae, has been removed by assuming a constant velocity versus density scaling factor (i.e., $\rho = a\beta$ where a is arbitrary). At this stage, we also apply a correction for geometrical spreading to convert from $R(t)$ to $s(t)$, the ray theoretical amplitude of the underside reflections. Note that the conversion from $V_s(t)$ to $s(t)$ is close to a derivative operator; the amplitude of $s(t)$ is proportional to the slope of $V_s(t)$. Step discontinuities in $V_s(z)$ predict delta functions in $s(t)$; the velocity gradients between the discontinuities also

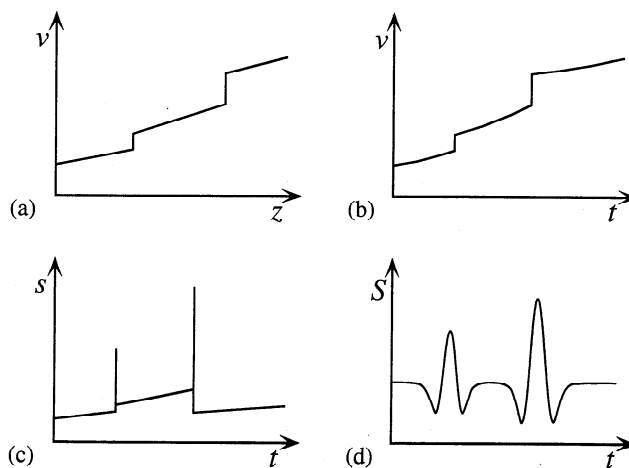### Forward modeling from velocity-depth profile

Figure 11. A cartoon illustrating the steps involved in computing the expected SS precursor time series from a velocity versus depth model. Assuming a reference range, ray theory is used to convert the $v(z)$ model (Figure 11a) into velocity as a function of the predicted arrival time of SS precursors for a reflector at depth z (Figure 11b). Assuming a constant velocity versus depth scaling factor, the amplitude of the precursors as a function of time $s(t)$ (Figure 11c) is then computed from the reflection coefficients derived from each velocity change (corrections for geometrical spreading are also applied at this point). Finally, $s(t)$ is convolved with the reference pulse to form the final synthetic seismogram, $S(t)$ (Figure 11d).

predict reflected energy (which will only be detected in data at suitably long periods).

The final step is to convolve the $s(t)$ function with the reference pulse to generate a realistic synthetic seismogram, $S(t)$ (Figure 11d). The SS reference pulse (see Figure 8) is band limited with little energy below 100-s period or above 10-s period. Thus the sharp features in $s(t)$ are smoothed, and the longest-period features are filtered out.

Before comparing this synthetic trace to the data stack of SS precursors, some additional corrections must be made. The SdS and SS pulse shapes are not identical, owing to the effects of the crust and extra attenuation on SS (see above). By convolving the SdS arrivals in the data with a suitable attenuation and crustal operator to match the SS arrival, a more accurate comparison with the synthetics is possible (the alternative, deconvolving the SS reference pulse prior to convolving with $s(t)$ in the synthetics, is less desirable, due to instabilities in the deconvolution). Another complication is that the stacking procedure, which aligns SS, will misalign the individual SdS arrivals slightly, because of time shifts in the $SS - SdS$ times caused by lateral heterogeneity and discontinuity topography. This scatter in the times will tend to attenuate the stacked SdS waveforms. Following *Revenaugh and Jordan* [1989, 1991], we assume these time shifts are normally distributed with standard deviation σ and convolve the synthetic SdS waveforms with the appropriate operator.

The attenuation correction uses a t^* operator ($t^* \sim$ 2 s) that accounts for the additional attenuation accumulated along SS between the surface and 550 km. Its main effect is to reduce the amplitude of the SdS peaks (for proper comparison with the SS pulse) and to shift them slightly in time to adjust for the difference between long-period velocities and the 1-Hz reference velocity in the Preliminary Reference Earth Model (PREM). Since most of the attenuation in PREM is concentrated at shallow depths, the SS to SdS attenuation differences may be reasonably approximated with a single correction computed for 550 km depth. The crustal correction assumes a 6-km-thick crust and has virtually no effect on the waveforms. Changes in the incoherent stacking parameter σ have a substantial effect on SdS amplitudes, with reductions of 11%, 22%, and 34% resulting from σ values of 2, 3, and 4 s. Unfortunately, obtaining a precise measure of σ is difficult. *Revenaugh and Jordan* [1991] estimated that $\sigma = 4.0 \pm 1.0$ s for the 660-km reflector in their ScS reverberation data. However, this result is for mixed continental and oceanic paths and includes the effects of heterogeneity throughout the mantle and thus is probably an overestimate for $SS - SdS$ times from oceanic bounce points.

To estimate σ for $SS - SdS$, I analyzed apparent depths to the 660-km discontinuity at different SS bounce point caps from a global study of discontinu-

ity topography [*Shearer*, 1993]. Using values uncorrected for crustal thickness or lateral heterogeneity, the standard deviation of the discontinuity depths is 10 km for global caps and 7 km for purely oceanic caps. Assuming that small-scale time shifts within each cap are comparable to the differences between the caps (consistent with the interpath versus intrapath results of *Revenaugh and Jordan* [1991]), this implies that $\sigma = 2.5$ s for $SS - S660S$ on individual seismograms. Since the bulk of upper mantle heterogeneity is above 400 km and the observed topography on the 410-km discontinuity is roughly comparable in amplitude to the 660-km topography [*Shearer*, 1993], $\sigma = 2.5 \pm 0.5$ s is a reasonable approximation to use for correcting the SdS waveforms.

Figure 12 plots the predicted $s(t)$ and $S(t)$ functions for the PREM and IASP91 velocity models [*Dziewonski and Anderson*, 1981; *Kennett*, 1991] compared to the data stack. Both models are adjusted to have a 6-km-thick crust, with the crust-ocean interface at 3 km depth. The comparison is made at 138°, the average range of the stacked records. As discussed above, the data trace has been convolved with attenuation and crustal operators (reducing the amplitude of the peaks compared to Figure 9); the synthetic trace has been convolved with a Gaussian function of $\sigma = 2.5$ s. Note the significant misfit between these models and the data. The timing and amplitude of the 410- and 660-km peaks are slightly off, and the models lack the 520-km peak,
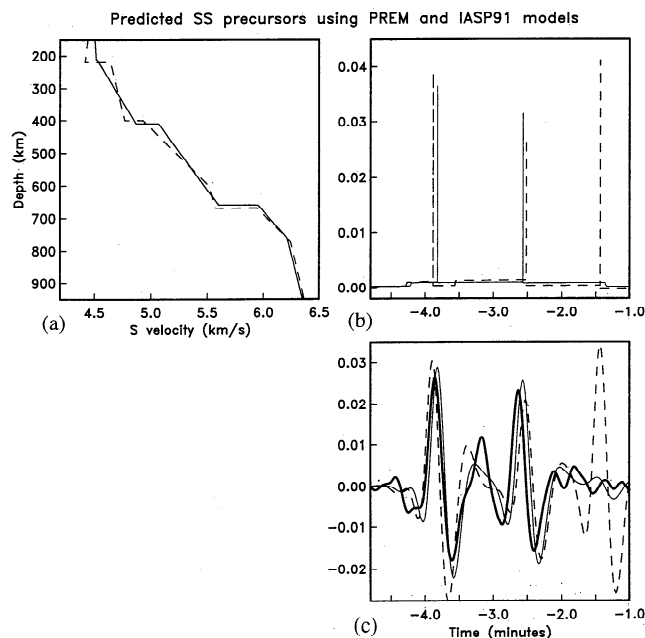

Figure 12. The fit to the SS precursor stack predicted by the PREM (dashed line) and IASP91 (solid line) velocity models. (a) S velocity versus depth for the two models. (b) Predicted ray theoretical amplitudes, $s(t)$, of the SS precursors, prior to convolving with the reference pulse shape. (c) The final synthetic seismograms (after convolution with the SS reference pulse), compared to the data stack (heavy solid line). Note the significant misfits between these models and the data.

as expected, since neither model contains structure at 520 km. The negative sidelobe before the 660-km peak at -3.9 min is wider and shallower in the data than the model predictions. PREM contains a large discontinuity at 220 km that is not seen in the data.

A much better fit to the SS precursors can be achieved with fairly small adjustments to the oceanic IASP91 model between 410 and 727 km depth. Figure 13 shows the results for model SSFIT1, which was achieved via trial and error forward modeling. Relative to IASP91, SSFIT1 contains smaller velocity contrasts near 410 and 660 km, a minor discontinuity near 520 km, and a steeper velocity gradient below 660 km (no attempt is made to fit the possible 280-km discontinuity). The S velocity jumps from 4.889 to 5.057 $km\,s^{-1}$ at 421 km (3.37% change), from 5.267 to 5.343 $km\,s^{-1}$ at 519 km (1.44% change), and from 5.645 to 5.931 $km\,s^{-1}$ at 663 km (4.95% change). Since a constant velocity ver-

sus density scaling was assumed in the modeling, the impedance changes at the discontinuities are twice these values. Below 666 km, the velocity increases rapidly to 6.19 $km\,s^{-1}$ at 727 km before rejoining the IASP91 velocities. Both the PREM and IASP91 models contain a steep S velocity gradient just below the 660-km discontinuity. The existence of such a layer is supported by the SS precursor data, but with a stronger gradient spread over a narrower zone than in either model. Error estimates on the discontinuity impedance changes may be obtained from the limits plotted in Figure 8 and the probable uncertainties in σ; these are $6.7 \pm 1.1\%$ at 421 km, $2.9 \pm 0.7\%$ at 519 km, and $9.9 \pm 1.5\%$ at 663 km.

These discontinuity depth estimates of 421 and 663 km are deeper than the average values of 413 and 653 km obtained from the *Shearer* [1993] global SS precursor study. Most of the difference results from the fact that the average S velocity between the Moho and the transition zone in the IASP91 model (used by SSFIT1 for the structure above 400 km) is slightly higher than the analogous velocity in PREM. This difference causes the discontinuities to move to greater depths to produce the same $SS - SdS$ times. Variations in reference upper mantle velocity models introduce differences in discontinuity depths of 5 to 10 km and are the largest source of uncertainty in absolute discontinuity depth estimates. The thickness of the layer between the 410- and 660-km discontinuities is better constrained, since most of the differences between velocity models are at depths shallower than 410 km.

Model SSFIT1 is designed to be as simple as possible while still giving a reasonable fit to the data and satisfying other known seismic constraints on transition zone structure. Since high-frequency reflections suggest sharp interfaces near 410 and 660 km [e.g., *Engdahl and Flinn*, 1969; *Benz and Vidale*, 1993], the model is parameterized in terms of velocity discontinuities separated by linear velocity gradients. The average model velocities cannot deviate too strongly from IASP91 or PREM; otherwise, teleseismic S wave travel time data would be misfit. Many other models can achieve fits as good, or even better, than the fit shown in Figure 13. For example, the velocity discontinuities could be replaced by steep velocity gradients with thicknesses up to about 50 km (long-period data cannot distinguish between velocity discontinuities and enhanced velocity gradients). A somewhat better fit to the negative sidelobes around the 520-km peak could be achieved by adding minor discontinuities or other structure to the velocity gradients above and below the 520-km discontinuity. Some of the velocity increase between 663 and 727 km could be accommodated with a minor velocity discontinuity near 720 km (as suggested by *Revenaugh and Jordan* [1991] for some of their ScS reverberation data), and it is possible to obtain a slightly better fit to the data by including such a feature. These complications are not included in the present model since they are not required within the probable uncertainties
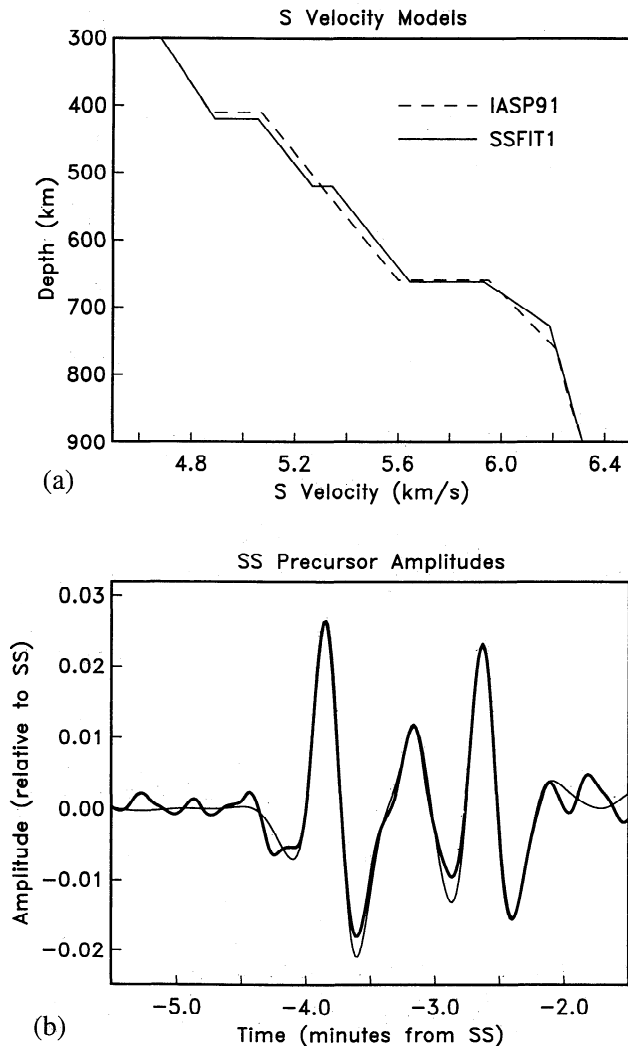

Figure 13. (a) S velocity versus depth for model SSFIT1 (derived in this paper) and IASP91. The models agree above 410 km and below 727 km. (b) Predicted SS precursors for SSFIT1 (thin line) compared to the data stack (heavy line).

of the data, nor are they seen in the $P'P'$ study of *Benz and Vidale* [1993].

SSFIT1 represents an average oceanic transition zone model, just as the stack shown in Figure 8 is an average over oceanic SS bounce points. Significant lateral velocity heterogeneity is certainly present in the transition zone, and it is not required that the velocity profile for any particular geographic region agree with the oceanic average. The differences between the northern and southern hemisphere stacks (Figure 10) caution against attempting to overinterpret minor features.

The Inverse Problem for v(z)

Given an SS precursor stack, can one invert directly for an upper mantle velocity model? The answer is yes, but the solution is nonunique, owing to the limited bandwidth of the data. The inverse problem may be described by considering the steps shown in Figure 11 in reverse order. From the data stack $S(t)$, the first step is to deconvolve the SdS waveforms with the reference SS pulse (as in the forward problem, we first apply an attenuation and crustal operator to the SdS time series so that the pulse shapes will agree with SS). Since the SS reference pulse is bandlimited ($\sim$10 to 100 s), this deconvolution will have no unique solution. The lack of high frequencies prevents resolving the upper mantle velocity discontinuities as sharp features, while the absence of low frequencies prevents imaging of the background upper mantle velocity gradient.

Figure 14 shows the results of applying deconvolution to the SS precursor stack. Using simple spectral deconvolution with a low-pass filter produces the trace in Figure 14a. The 410-, 520-, and 660-km peaks are clearly apparent but are embedded in long-period noise. The long-period drift could be eliminated by applying a high-pass filter. However, this would introduce troughs around the discontinuity peaks, features that are not required by the data but are artifacts of the deconvolution method (this is a common problem with deconvolution; see, for example, *Sipkin and Lerner-Lam* [1992]). To avoid this difficulty, I fit the long-period drift in Figure 14a with a simple spline curve and subtracted this from the trace to produce Figure 14b (corresponding to the $s(t)$ function shown in Figure 11c). Figure 14c shows the fit achieved to the original SdS stack when this trace is convolved with the reference pulse. The fit is not perfect, owing mainly to the smoothing effect of the low-pass filter.

The next step is to map $s(t)$ into $v(z)$. This is done beginning at the top of the $v(z)$ model. Consider a point in the $v(z)$ model that corresponds to an underside SS reflection at time t_0. The amplitude $s(t_0)$ can be corrected for geometrical spreading to give the reflection coefficient at z_0. Given the local ray angle and assuming a constant velocity versus density scaling relationship, the velocity change dv can be obtained from the reflection coefficient. Finally, the difference in depth dz is
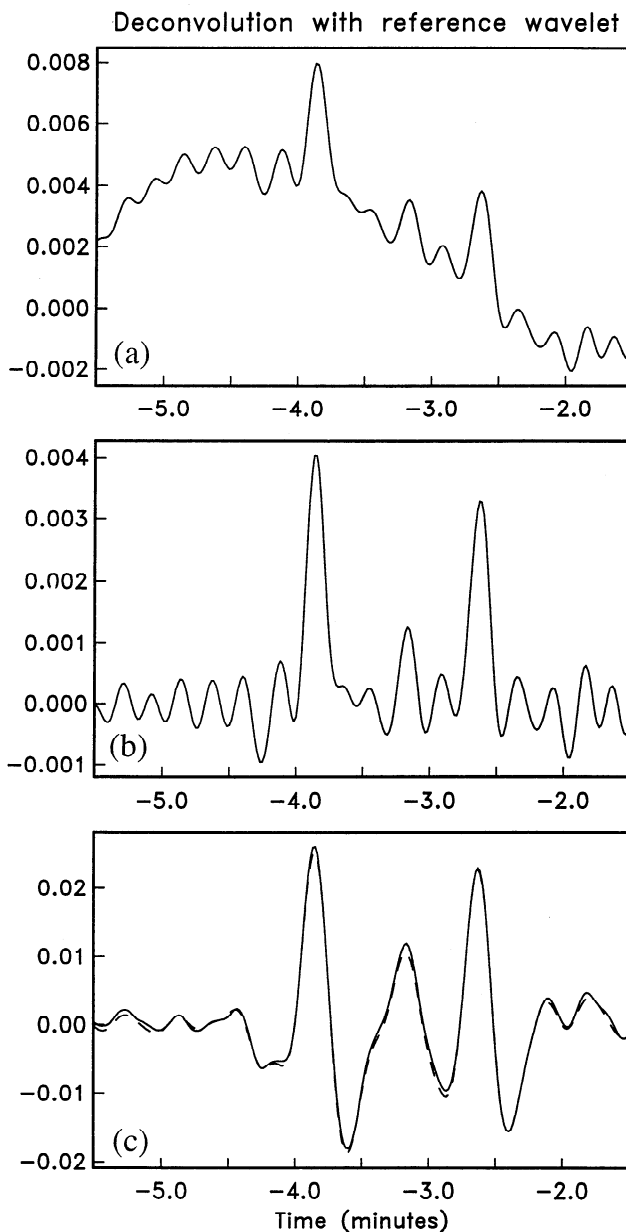

Figure 14. (a) The stacked SS precursors, following spectral deconvolution with the SS reference pulse. (b) The deconvolved SS precursors with the long-period drift removed by fitting a spline to the trace in Figure 14a. (c) The dashed line shows the fit achieved to the data stack (solid line) after convolving the trace in Figure 14b with the SS reference pulse.

found that changes the SdS travel time by dt, the digitization interval ($dt = 1$ s for these data). This gives us a new point on the $v(z)$ curve at $z = z_0 + dz, v = v_0 + dv$ and a new time in the $s(t)$ function ($t = t_0 + dt$).

If this procedure were applied directly to the $s(t)$ trace shown in Figure 14c, the result would be unrealistic since the negative parts of $s(t)$ would lead to velocity decreases with depth, and there would be no general background upper mantle velocity increase with depth. We can avoid this difficulty by adding a constant function to $s(t)$ so that the background $v(z)$ gradient agrees

with IASP91. After some experimentation, a ramp function (decreasing from 0.001 at 0 km to 0.00065 at 1000 km) was found to give reasonable results. Figure 15 shows the final S velocity model obtained, compared to the IASP91 model. Enhanced velocity gradients are resolved near 420, 520, 670, and 740 km. Below about 800 km depth, the velocity begins increasing rapidly to unrealistic values. This results from an instability in the inversion that is caused by the reduced reflection coefficients predicted for the increasingly horizontal ray incidence angles at increasing depth. To compensate for the smaller predicted reflection coefficients, the computed velocities must increase. This difficulty could be avoided by reducing the ramp function added to $s(t)$ at these times but at the cost of further complicating the inversion procedure.

The velocity model plotted in Figure 15 contains intervals of steep velocity gradients 30- to 50-km thick, rather than sharp discontinuities. This is not evidence against sharp features; long-period SdS reflections cannot distinguish between discontinuities and enhanced velocity gradients, and the data could be fit equally well with sharp interfaces. The pulse broadening and amplitude reductions related to incoherent stacking (discussed in the previous section) are not directly addressed in this inversion approach; these effects are absorbed into the final $v(z)$ model. Thus a model with perfectly sharp discontinuities would not be expected, since time shifts due to lateral heterogeneity and discontinuity topography would spread out the velocity increases, even if the discontinuities were locally sharp.
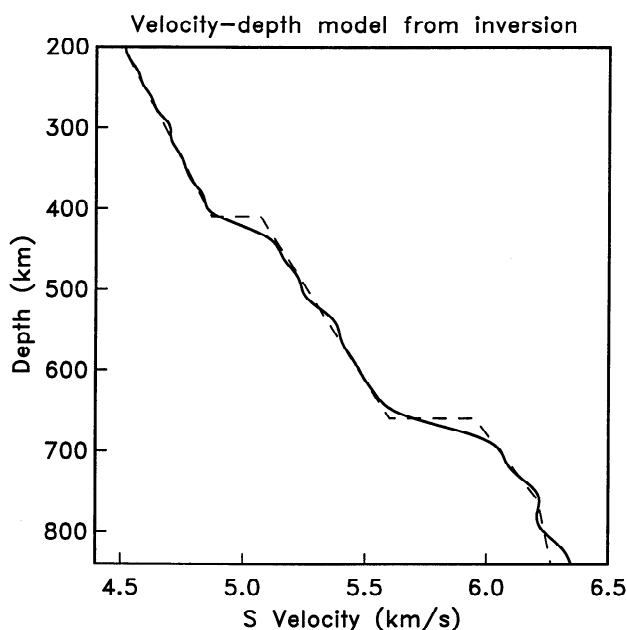
The inverse procedure described here has the advantage of directly producing a $v(z)$ model that gives a good fit to the SS stack, without any prior assumptions regarding discontinuity depths. The results provide additional support for the existence of a 520-km discontinuity. However, the method is not free of subjectivity, since smoothness constraints must be imposed on the deconvolution and the overall slope of the $v(z)$ curve adjusted to match standard models. Incorporating prior constraints on the model is tricky without resorting to ad hoc approaches. For example, it is difficult to force the discontinuities to be sharp without introducing high-frequency artifacts at other depths in the model.

Discussion

Both the forward and inverse modeling approaches described here assume that the SS precursor waveforms are known for a single reference trace at a specific range (138° in the examples presented). However, the stacking procedure used to produce this trace combines and averages data from different ranges (120° to 160°) and provides only an approximation to the true response at 138°. Some pulse broadening will occur, since the $S410S$ and $S660S$ travel time curves are not perfectly parallel to the $S550S$ reference curve used in the stacking. However, this effect is small compared to the spreading that occurs due to lateral heterogeneity and topography (see above); time shift errors from using $S550S$ never exceed 2.5 s for either the 400- or 660-km peaks, with most errors being much smaller.

SH reflection coefficients vary as a function of both impedance contrast and ray angle. For a fixed impedance jump, reflected amplitudes are reduced for deeper discontinuities and shorter ranges where the incident ray angles become more horizontal. This effect was ignored in the SS amplitude analysis in the work by *Shearer* [1991], which incorrectly assumed that the reflection coefficients could be adequately approximated by the values at vertical incidence. The almost equal amplitudes of the $S410S$ and $S660S$ phases do not imply nearly equal impedance jumps at 410 and 660 km. Instead, a higher impedance jump is required at 660 km to compensate for the reduced reflection coefficient caused by the more oblique incidence angle. For model SSFIT1, the 410/660 impedance ratio is about 0.7, close to the *Revenaugh and Jordan* [1991] value of 0.6 obtained from ScS reverberations.

Since predicted SdS/SS amplitudes vary as a function of range, by averaging records between 120° and 160°, the stacking technique provides an approximation to the amplitude at 138°. SdS amplitudes are smaller at 120° than at 160°, but the amplitude variations are not severe ($S660S$ is substantially weaker at 110°; this is one reason the 110° to 120° data are excluded from the final stack). A possible improvement to the stacking method described here would be to first convert

Figure 15. The S velocity versus depth model obtained from the deconvolved SS precursor stack, compared to the IASP91 model (dashed line). As a result of the limited bandwidth of the long-period data, this model contains regions of enhanced velocity gradient rather than sharp discontinuities.

each individual seismogram to discontinuity impedance change versus depth, using the ray geometry appropriate to each range, and then to stack to obtain an average impedance versus depth function. This would have some similarities to the approach used by *Revenaugh and Jordan* [1989, 1991] in their *ScS* reverberation work and has the advantage of explicitly accounting for the range dependence of *SdS* times and amplitudes. However, a complication in this technique is that the reference pulse shape would no longer be related directly to the pulse shapes of the discontinuity reflections in the stacked trace, making both the forward and inverse problems for $v(z)$ more difficult. This could be avoided by deconvolving *SS* from each trace prior to stacking, but this would increase the ambiguities associated with deconvolution, particularly since the edges of the *SS* pulse are not always clearly defined on individual seismograms.

The resolution of the $v(z)$ models obtained in this analysis are fundamentally limited by the narrow bandwidth of the long-period GDSN data. By using broadband data, future studies may be able to extend these results to both higher and lower frequencies. At higher frequencies, improved imaging of the sharpness of upper mantle discontinuities would be possible, although increased noise and waveform incoherence may limit the effectiveness of waveform stacking. At lower frequencies, the results will become more sensitive to the steepness of the velocity gradients between the discontinuities. The resolution of the *SS* precursor stack described here, although limited, is still sufficient to discriminate between many different upper mantle velocity models. The results may prove useful in hypothesis testing of models derived from other seismic or mineral physics constraints. In principle, the same techniques could be applied to obtain upper mantle P velocity models using PP precursors and/or topside P multiples.

The 520-km Discontinuity

Long-period 520-km reflections have been detected as topside reflections following P and S [*Shearer*, 1990, 1991], underside reflections preceding SS (see *Shearer* [1991] and this paper), and in *ScS* reverberations [*Revenaugh and Jordan*, 1991]. Given the consistency of these observations, it is interesting that a 520-km reflector has not been detected in short-period $P'P'$ precursors [*Benz and Vidale*, 1993] or in several detailed seismic refraction studies [e.g. *Cummins et al.*, 1992; *Jones et al.*, 1992]. The Benz and Vidale $P'P'$ study showed very clear 410- and 660-km reflections and limits the 520-km discontinuity, at least in one location, to widths greater than 10 km so that it is invisible to short-period reflections. The sensitivity of the refraction studies to minor velocity changes is not clear, and it is possible that velocity changes of a percent or less could be missed. A recent analysis of long-range records from Russian nuclear explosions found evidence for a

550-km discontinuity on two of the profiles [*Mechie et al.*, 1993].

All of the available seismic observations can be reconciled with a global 520-km "discontinuity," if this feature is between 10 and 50 km in thickness and has changes in velocity small enough to avoid routine detection in refraction studies. This study suggests an S impedance change, $\Delta\rho V_s$, near 520 km of about 2.2–3.6%, while the 520-km reflectors seen in the *ScS* reverberation study of *Revenaugh and Jordan* [1991] indicated $\Delta\rho V_s$ values of 2.8–4.0%. These impedance changes can be partitioned into different velocity and density jumps, since the reflection coefficients depend only upon the product of velocity and density. The lack of routine observations of a 520-km velocity discontinuity in refraction studies suggests that the bulk of the impedance change occurs in density rather than velocity.

Support for this interpretation comes from mineral physics results for the β to γ phase change in olivine, the leading candidate to explain the 520-km discontinuity since it occurs at the appropriate pressure. For pure olivine, *Rigden et al.* [1991] obtained $\Delta V_p = 1$–2%, $\Delta V_s = 0.8$–1.5%, and $\Delta\rho = 2.5$–3% over a depth interval of ~50 km. The corresponding P and S impedance jumps are 3.5–5% and 3.3–4.5%, respectively, with most of the change occurring in density rather than velocity. Assuming that $\Delta\rho V_s = 2.2$–3.6% near 520 km in the upper mantle (this study), that $\Delta\rho V_s = 3.3$–4.5% for the olivine β to γ phase change, and that this phase change is the only contributor to the 520-km impedance jump, then the fraction of olivine in the transition zone must be greater than 50%, supporting olivine-rich (i.e., pyrolite) models of mantle composition [e.g., *Ita and Stixrude*, 1992; *Bina*, 1993].

References

Benz, H.M., and J.E. Vidale, Sharpness of upper-mantle discontinuities determined from high-frequency reflections, *Nature*, *365*, 147–150, 1993.

Bina, C., Mutually consistent estimates of upper mantle composition from seismic velocity contrasts at 400 km, *Pure Appl. Geophys.*, *141*, 101–109, 1993.

Bock, G., Synthetic seismogram images of upper mantle structure: No evidence for a 520-km discontinuity, *J. Geophys. Res.*, *99*, 15,843–15,851, 1994.

Bock, G., and R. Kind, A global study of S-to-P and P-to-S conversions from the upper mantle transition zone, *Geophys. J. Int.*, *107*, 117–129, 1991.

Cummins, P.R., B.L.N. Kennett, J.R. Bowman, and M.G. Bostock, The 520-km discontinuity, *Bull. Seismol. Soc. Am.*, *82*, 323-336, 1992.

Davis, J.P., R. Kind, and I.S. Sacks, Precursors to P′P′ re-examined using broad-band data, *Geophys. J. Int.*, *99*, 595–604, 1989.

Dziewonski, A.M., and D.L. Anderson, Preliminary reference Earth model, *Phys. Earth Planet. Inter.*, *25*, 297–356, 1981.

Efron, B., and R. Tibshirani, Statistical data analysis in the computer age, *Science*, *253*, 390–395, 1991.

Engdahl, E.R., and E.A. Flinn, Seismic waves reflected from discontinuities within Earth's upper mantle, *Science*, *163*, 177–179, 1969.

Ita, J., and L. Stixrude, Petrology, elasticity, and composition of the mantle transition zone, *J. Geophys. Res.*, *97*, 6849–6866, 1992.

Johnson, L.R., Array measurements of P velocities in the upper mantle, *J. Geophys. Res.*, *72*, 6309–6325, 1967.

Jones, L.E., J. Mori, and D.V. Helmberger, Short-period constraints on the proposed transition zone discontinuity, *J. Geophys. Res.*, *97*, 8765–8774, 1992.

Kennett, B.L.N. (ed.), *IASPEI 1991 Seismological Tables*, Res. Sch. of Earth Sci., Aust. Nat. Univ., Canberra, 1991.

Kind, R., and L.P. Vinnik, The upper-mantle discontinuities underneath the GRF array from P-to-S converted phases, *J. Geophys.*, *62*, 138–147, 1988.

Mechie, J., A.V. Egorkin, K. Fuchs, T. Ryberg, L. Solodilov, and F. Wenzel, P-wave mantle velocity structure beneath northern Eurasia from long-range recordings along the profile Quartz, *Phys. Earth Planet. Inter.*, *79*, 269–286, 1993.

Niazi, M., and D.L. Anderson, Upper mantle structure of western North America from apparent velocities of P waves, *J. Geophys. Res.*, *70*, 4633–4640, 1965.

Paulssen, H., Evidence for a sharp 670-km discontinuity as inferred from P-to-S converted waves, *J. Geophys. Res.*, *93*, 10,489–10,500, 1988.

Revenaugh, J., and T.H. Jordan, A study of mantle layering beneath the western Pacific, *J. Geophys. Res.*, *94*, 5787–5813, 1989.

Revenaugh, J., and T.H. Jordan, Mantle layering from ScS reverberations, 2, The transition zone, *J. Geophys. Res.*, *96*, 19,763–19,780, 1991.

Richards, M.A., and C.W. Wicks, S–P conversion from the transition zone beneath Tonga and the nature of the 670-km discontinuity, *Geophys. J. Int.*, *101*, 1–35, 1990.

Rigden, S.M., G.D. Gwanmesia, J.D. FitzGerald, I. Jackson, and R.C. Liebermann, Spinel elasticity and seismic structure of the transition zone of the mantle, *Nature*, *354*, 143–145, 1991.

Shearer, P.M., Seismic imaging of upper-mantle structure with new evidence for a 520-km discontinuity, *Nature*, *344*, 121–126, 1990.

Shearer, P.M., Constraints on upper mantle discontinuities from observations of long-period reflected and converted phases, *J. Geophys. Res.*, *96*, 18,147–18,182, 1991.

Shearer, P.M., Global mapping of upper mantle reflectors from long-period SS precursors, *Geophys. J. Int.*, *115*, 878–904, 1993.

Shearer, P.M., and G. Masters, Global mapping of topography on the 660-km discontinuity, *Nature*, *355*, 791–796, 1992.

Sipkin, S.A., and A.L. Lerner-Lam, Pulse-shape distortion introduced by broadband deconvolution, *Bull. Seismol. Soc. Am.*, *82*, 238–258, 1992.

Vidale, J.E., and H.M. Benz, Upper-mantle discontinuities and the thermal structure of transition zones, *Nature*, *356*, 678–681, 1992.

Wicks, C.W., and M.A. Richards, A detailed map of the 660-kilometer discontinuity beneath the Izu-Bonin subduction zone, *Science*, *261*, 1424–1427, 1993.

Zhang, Z., and T. Lay, Investigation of upper mantle discontinuities near northwestern Pacific subduction zones using precursors to sSH, *J. Geophys. Res.*, *98*, 4389–4405, 1993.

P. M. Shearer, Institute of Geophysics and Planetary Physics, Scripps Institution of Oceanography, University of California, San Diego, La Jolla, CA 92093-0225. (e-mail: pshearer@ucsd.edu)